

A STUDY OF MIXING AND INTERMITTENCY IN A COAXIAL TURBULENT JET

K.K.J.Ranga Dinesh¹, A.M.Savill¹, K.W.Jenkins¹, M.P.Kirkpatrick²

ABSTRACT

A Large Eddy Simulation study of mixing and intermittency of a coaxial turbulent jet discharging into an unconfined domain has been conducted. The work aims to gain insight into the mixing and intermittency of turbulent coaxial jet configurations. The coaxial jet considered has relatively high jet velocities for both core and annular jets with an aspect ratio (core jet to annular jet) of 1.48. The computations resolved the temporal development of large-scale flow structures by solving the transport equations for the spatially filtered mass, momentum and passive scalar on a non-uniform Cartesian grid and employed the localised dynamic Smagorinsky eddy viscosity as a subgrid scale turbulence model. The results for the time-averaged mean velocities, associated turbulence fluctuations, and mean passive scalar fields are presented. The initial inner and outer potential cores and the shear layers established between two cores have been resolved together with the establishment of high turbulence regions between the shear layers. The passive scalar fields developing from the core and bypass flow were found to exhibit differences at near and far field locations. Probability density distributions of instantaneous mixture fraction and velocity have been created from which intermittency has been calculated and the development of intermittency from the probability density distributions for instantaneous velocity follow similar variations as for the passive scalar.

Key Words: Coaxial jet, Mixing, Intermittency, LES

1. INTRODUCTION

The study of mixing structure and intermittent behaviour of a coaxial jet discharging from a circular inlet to free space is important for many practical engineering applications such as aeroacoustic, propulsion and environmental emissions. In addition, coaxial jet motion is often used as a mechanism to promote or control mixing between a fuel spray jet and the adjacent air for combustion applications, as well as to control the turbulent transport within a jet region. Since coaxial jet mixing can have a profound effect on self-similarity and downstream mixing in applied engineering systems, a detailed understanding of the mixing and its inter related processes such as turbulent intermittency characteristics is beneficial to the design process.

During the past few decades various experimental studies have been carried out to investigate the characteristics of coaxial jets; mainly focusing on mixing of both passive and active scalars, the shear layers between the inner and outer jets, and the influence of the inlet conditions on mixing properties. Regarding experimental investigations; Forstall and Shapiro (1951) first studied the effects of different inlet velocity ratios on mixing and concluded that the velocity ratio is more important to determine the near and far field mixing of coaxial jets. Chigier and Beer (1964) studied the near nozzle flow region in double concentric jets. Ko and Kwan (1971) and Kwan and Ko (1977) carried out subsonic coaxial jet studies and divided the near field into different zones, while defining the mixing regions with demonstration of similarities between coaxial and single jets. Dahm et al. (1992) conducted comprehensive flow visualisation for coaxial jets and found a variety of near field vortex patterns. Buresti et al. (1998) investigated the near field flow properties of

coaxial jets and demonstrated the relation between inlet wall thickness and vortex shedding phenomena. Sadr and Klewicki (2003) also studied the near field flow development in coaxial jets and described the anisotropic turbulence structure in the inner mixing layer. At the same time a series of intermittency measurements have also been made for some turbulent jets. For example, Becker et al. (1965) investigated scalar intermittency in jets and Wygnanski and Fiedler (1969) obtained intermittency data for a self-preserving high Reynolds number axisymmetric turbulent jet. Bilger et al. (1976) also took intermittency experimental data for the temperature field using the probability density function (PDF) approach, while Shefer and Dibble (2001) investigated intermittency for propane based round jet.

Numerical investigation of a spatially evolving coaxial turbulent jet has also received considerable attention. The continuous development of high performance computing and large core memories has facilitated the performance of large scale simulations respecting both spatial and time accuracy. This has allowed both direct numerical simulation (DNS) and large eddy simulation (LES) techniques to be employed especially for more fundamental investigations. In the DNS all the length and time scales of turbulence are directly resolved and hence no turbulence models are required, but currently this technique is only applicable for relatively low Reynolds number flows. In LES only large scales of turbulence are directly computed with the effect of the small scales requiring a turbulence model.

Several large scale DNS studies have been carried out for coaxial jet calculations. For example, da Silva and Metais (2001) conducted DNS of the spatially evolving coaxial round jets, and da Silve et al. (2003) studied the transition in high velocity ratio

coaxial jets using DNS. Balarac and Metais (2005) also studied the near field of coaxial jets using DNS and analysed the influence of the inner shear layer for the momentum thickness of jet nozzle. Balarac et al. (2007) further extended their DNS work and simulated the high velocity ratio coaxial jets with various upstream conditions. LES is capable of simulating higher Reynolds number flows and hence many jet simulations have been carried out successfully using now affordable computing power. For example, Akselvoll and Moin (1996) have performed LES calculations of confined coaxial jets and discussed fluid dynamical aspects of confined coaxial jets. Boersma and Lele (1999) performed another LES calculation for a compressible round jet. Yuan et al. (1999) reported a separate series of LES calculations for a round jet issuing normally into a cross flow. Dianat et al. (2006) performed LES of scalar mixing in a coaxial jet, and Tucker (2008) examined various LES submodels for a round jet type configuration with the aim of predicting jet noise.

A few attempt also been made to perform intermittency modelling of free shear flows using classical Reynolds averaged Navier-Stokes (RANS) techniques. For example, Byggstoyl and Kollmann (1981) studied the intermittency of a round jet using a $k - \varepsilon$ model and Kollmann and Janicka (1982) analysed the intermittency using a transport probability density function (PDF). Cho and Chung (1992) also developed more economical intermittency model by incorporating intermittency transport equation to already exist $k - \varepsilon$ turbulence model.

Despite the success of the above noted investigations on free shear flows, further studies for the mixing and its inter related topics such as turbulent intermittency are vital. The applicability of large eddy simulation technique for the prediction of

turbulent intermittency is one such issue. The objective of the present work is therefore to study the mixing process and intermittent characteristics of a turbulent coaxial jet in isothermal incompressible conditions using a localised dynamic sub-grid model version of the large eddy simulation technique. The configuration considered here is a scaled version of a typical RB211 aero engine exhaust using the engine characteristics provided by Garnier et al. (1997). We have focused on predicting probability density functions and turbulent intermittency of both velocity and passive scalar fields under constant density, non-reacting, incompressible conditions. The present effort can be considered as an essential step in developing understanding for the extension of LES sub-grid scale models to explicitly consider intermittency effects in constant density and variable density flow conditions with an ultimate aim of improving simulations for aircraft engine emissions.

The remainder of the paper is organised as follows: in section 2, we discuss the governing equations and modelling. In section 3, we describe the numerical setup for separate simulations. Section 4 discusses the results from these simulations and analyses the mixing and intermittency for both velocity and passive scalar fields. Final conclusions are presented in section 5.

2. GOVERNING EQUATIONS

In LES the large-scale energy containing scales of motion are resolved numerically while the small, unresolved scales and their interactions with the large scales are modelled. The grid-filtering operator, known as a spatial filter, is applied to decompose the resolved and sub-grid scales in the computational domain. Applying the spatial box filter to incompressible governing equations, we obtain the filtered

continuity, momentum and passive scalar equations for the large-scale motion as follows:

$$\frac{\partial \bar{u}_j}{\partial x_j} = 0, \quad (1)$$

$$\frac{\partial \bar{u}_i}{\partial t} + \frac{\partial (\bar{u}_i \bar{u}_j)}{\partial x_j} = -\frac{1}{\rho} \frac{\partial \bar{P}}{\partial x_i} + \frac{\partial (2\nu \bar{S}_{ij})}{\partial x_j} + \frac{\partial (\tau_{ij})}{\partial x_j}, \quad (2)$$

$$\frac{\partial \bar{c}}{\partial t} + \frac{\partial (\bar{u}_j \bar{c})}{\partial x_j} = \left(\frac{\nu}{\sigma} + \frac{\nu_t}{\sigma_t} \right) \frac{\partial^2 \bar{c}}{\partial x_j \partial x_j}, \quad (3)$$

Where $u_i, \rho, p, \nu, c, \sigma$ and σ_t denote the velocity, density, pressure, kinematic viscosity, passive scalar concentration, laminar and turbulent Schmidt numbers, and the strain rate tensor, $S_{ij} = \frac{1}{2} \left(\frac{\partial \bar{u}_i}{\partial x_j} + \frac{\partial \bar{u}_j}{\partial x_i} \right)$. The last term of equation (2) represents the sub-grid scale (SGS) contribution to the momentum and it is known as the SGS stress tensor. Hence subsequent modelling is required for $\tau_{ij} = \left(\overline{u_i u_j} - \bar{u}_i \bar{u}_j \right)$ to close the system of equations.

The Smagorinsky (1963) eddy viscosity model is used here to model the SGS stress tensor $\tau_{ij} = \left(\overline{u_i u_j} - \bar{u}_i \bar{u}_j \right)$ such that

$$\tau_{ij} - \frac{1}{3} \delta_{ij} \tau_{kk} = -2\nu_{sgs} \bar{S}_{ij} \quad (4)$$

Here the eddy viscosity ν_{sgs} is a function of the filter size and strain rate

$$\nu_{sgs} = C_s \bar{\Delta}^2 |\bar{S}| \quad (5)$$

Where C_s is a Smagorinsky (1963) model parameter and $|\bar{S}| = (2\bar{S}_{ij}\bar{S}_{ij})^{\frac{1}{2}}$. In the present study the localised dynamics procedure of Piomelli and Liu (1995) was used to obtain the model parameter C_s , which appears in equation (5) as a part of the SGS turbulence model.

3. NUMERICAL DETAILS

3.1 Computational domain, flow conditions and grid resolution

The coaxial jet considered has a core jet with diameter $D_c = 0.878m$, surrounded by an annular secondary jet with overall diameter $D_a = 1.422m$. The centre of the core flow is taken as the geometric centre line of the flow where $r = 0$ and $x = 0$. Two independent bulk velocities are used as inlet velocities for the simulations, the bulk axial velocity of core jet, $U_c = 158m/s$ and the bulk axial velocity of secondary annular inlet, $U_a = 104m/s$. The Reynolds number is defined in terms of the primary (bulk) axial velocity (U), diameter of the core jet annulus (D) and the kinematic viscosity of air ν such that $Re = UD/\nu$. The computational domain extended for 30 core jet diameters radially and 40 core jet diameters axially, corresponding to dimensions of $26m \times 26m \times 43m$ in the x,y and z directions respectively. To check grid sensitivity, two different grid resolutions have been used and results will be showed later. The inflow mean axial velocity distribution for the core flow was specified using the power law velocity profile such that

$$\langle U \rangle = C_0 U_j \left(1 - \frac{|r|}{r_c} \right)^{1/7} \quad (6)$$

where U_j is bulk velocity of the core jet, r is the radial distance from the jet centre line, and r_c is the radius of the core jet. A value for the constant $C_0 = 1.28$ was adopted, which is consistent with a fully developed turbulent pipe flow at outlet. A similar equation is used to specify the inlet axial velocity for the annular jet region with the radius of the annular jet replacing that of the core jet such that

$$\langle U \rangle = C_0 U_j \left(1 - \frac{|r|}{r_a} \right)^{1/7} \quad (7)$$

where U_j is bulk velocity of the annular jet, r is the radial distance from the jet centre line, and r_a is the radius of the annular jet and similar value is used for constant C_0 . Here we employed an artificial inflow condition to produce instantaneous velocity component U_{in} such that

$$U_{in}(x,t) = U_{Mean} + \theta(x,t)u'_{rms} \quad (8)$$

where U_{Mean} is the mean inflow velocity, u'_{rms} is the root mean square turbulent fluctuation and $\theta(x,t)$ is a random number having a Gaussian distribution. This approach should be sufficient at low inflow turbulence level and we have used this method successfully in previous investigations (Ranga Dinesh, 2007). Free slip boundary conditions were used for the side walls of the computational domain and convective boundary conditions are used at the outflow. For the passive scalar, a top hat profile was specified at the inlet such that in one case, the passive scalar value was 1.0 across the core inlet and zero elsewhere, and while for a second case the passive scalar value was 1.0 for the annular inlet, and zero elsewhere. For the scalar field a zero normal gradient condition was used at the outlet.

The time averaged mean axial and radial velocities, mean passive scalar components and their mean fluctuating values are calculated by time averaging the unsteady variables obtained from LES results, i.e.

$$\langle \bar{\phi} \rangle = \frac{1}{N_t} \sum_{n=1}^{N_t} \bar{\phi}^n, \quad \bar{\phi}_{rms} = \sqrt{\frac{1}{N_t} \sum_{n=1}^{N_t} (\bar{\phi}^n - \langle \bar{\phi} \rangle)^2} \quad (9)$$

Where N_t represents the number of samples.

The simulations were carried out for 10 flow passes (one flow pass indicates the total time for the inlet flow velocity to reach the outlet boundary) transiently, and then statistics were collected over another 10 flow passes. This allowed the flow field to fully develop and any initial transients to exit the computational domain. The samples for the statistical calculations were taken only after the flow field had been established to be fully developed.

3.2 Numerical discretisation

The program used to perform simulations is the PUFFIN code developed by Kirkpatrick et al. (2003a, b, 2005) and later extended by Ranga Dinesh (2007). PUFFIN computes the temporal development of large-scale flow structures by solving the transport equations for the spatially filtered continuity, momentum and passive scalar. The equations are discretised in space using the finite volume formulation in Cartesian coordinates on a non-uniform staggered grid. Second order central differencing (CDS) is used for the spatial discretisation of all terms in both the momentum equation and the pressure correction equation. This minimises the projection error and ensures convergence in conjunction with an iterative solver. The diffusion terms of the passive scalar transport equation are also discretised using the

second order CDS. The convection term of the scalar transport equation is discretised using the SHARP scheme (Leonard, 1987).

The time derivative of the mixture fraction is approximated using the Crank-Nicolson scheme. The momentum equations are integrated in time using a second order hybrid scheme. Advection terms are calculated explicitly using second order Adams-Bashforth, while diffusion terms are calculated implicitly using second order Adams-Moulton to yield an approximate solution for the velocity field. Finally, mass conservation is enforced through a pressure correction step. The time step is varied to ensure that the Courant number $C_o = \Delta t u_i / \Delta x_i$ remains approximately constant where Δx_i is the cell width, Δt is the time step and u_i is the velocity component in the x_i direction. The solution is advanced with a time stepping corresponding to a Courant number in the range of $C_o = 0.3$ to 0.5 . The Bi-Conjugate Gradient Stabilized (BiCGStab) method with a Modified Strongly Implicit (MSI) preconditioner is used to solve the system of algebraic equations resulting from the discretisation.

4. RESULTS AND DISCUSSION

In this section the results obtained from the LES computations are discussed. First we discuss the grid sensitivity study, followed by the velocity distributions and passive scalar distributions. The radial plots of the mean and rms quantities have been normalised by the diameter of the annular jet ($D_a = 1.422m$).

4.1 Grid sensitivity analysis

We have initially considered two grid resolutions to investigate the grid sensitivity. Grid 1 used $140 \times 140 \times 60$ grid points along x,y and z directions (approximately 1.2

million cells) and grid 2 used $140 \times 140 \times 120$ grid points along x,y and z directions (approximately 2.4 million cells). Fig. 1 shows the results for mean axial velocity (top), rms axial velocity (middle) and mean mixture fraction (bottom) at two different axial locations ($x/d=5.0, 10.0$). Here the dashed line indicates grid 1 (coarse grid) results and solid line indicates grid 2 (fine grid) results. It has been found that the near field comparisons from both grids show similar results whilst some differences are found at downstream axial locations. The peak values of the mean axial velocity and mean passive scalar are slightly higher for the coarser grid than finer grid. This shows that the grid resolutions along the axial direction (here z direction) has a direct impact on mixing of the two jets and in particular that the finer grid is able to capture more mixing than the coarser grid due to the higher grid resolution along the axial direction. All remaining results discuss in this section are thus based on finer grid (2.4 million) resolution simulations.

4.2 Analysis of results for velocity and scalar fields

4.2.1 Velocity Field:

Fig. 2 presents a contour plot of the mean axial velocity which shows the structure of the coaxial jet where we can see the extent of the potential core of the jet. The centreline mean axial velocity has minimal influence from the annular flow in near field, ($0 < x/D < 5.0$). As observed by Ko and Kwan (1971) the contour plot reveals the initial merging zone of both inner and outer potential cores, as well as the region immediately downstream (intermediate zone) where the inner and outer mixing regions merge. A close up view of the contour plot at near field shows the flow separation between inner and outer potential cores and also the inner and outer mixing regions.

Fig. 3 shows the radial plots of the mean axial velocity (left side) and root mean square (rms) axial velocity (right side) at different axial locations. The mean axial profiles show the expected axi-symmetric behaviour and the mean velocity profile in the core jet is consistent with a fully developed pipe flow profile. As mentioned by Buresti et al. (1998), the inlet velocity profile shape can significantly influence the coaxial jet characteristics from near to far field locations. Since we used a power law profile to specify the mean velocity at inlet, the velocity profiles play an important role in producing a weaker shear region in the core side of the inner mixing region. In addition, the shear layer regions are also affected by the velocity aspect ratio and further investigations of different aspect ratios would be beneficial to fully understand the mixing regions and various vortex patterns for coaxial jets in general. The present results however indicate a self-similar state is established at a closer distance to the jet exit plane. This has been also observed by Ribeiro and Whitelaw (1980) in their coaxial jet experiment. Although the core and annular jet have relatively high initial bulk velocities, the shape of the axial velocity decay agrees with other findings, e.g. Sadr and Klewicki (2003). Considering the velocity ratio between the core and annular jet regions ($U_c/U_0 = 1.48$), the length of the potential cores are consistent with previous findings for the velocity ratio $U_c/U_0 = 1.24$ (Sadr and Klewicki) and Ribeiro and Whitelaw (1980). The existence of higher mean axial velocity in the central region of the jet is related to higher production associated with the higher velocity ratio of 1.48. As seen in Fig. 3 the large gradients considered due to the velocity ratio in the mean axial profile lead to increased turbulence intensities as has been also observed by Champagne and Wygnanski (1971) for their coaxial jet experiment. The centreline rms axial velocity fluctuation has very small values near the centreline and then exhibits a double peak in the region ($0.3 \leq r/D \leq 0.5$). The

highest peak location occurs in the annular jet as a result of the vortex shedding in the inner mixing region between inner potential core and outer potential core. This has been observed by Sadr and Klewicki (2003). As noted by Champagne and Wygnanski (1971) regions with large mean axial velocity gradient contains high turbulence intensities and the present simulations confirm this finding. The sudden increase of the velocity fluctuations across the shear layer is an important aspect of the dynamics of the coaxial jet at such velocity aspect ratio as discussed in more detail by Dahm et al. (1992) who also studied a coaxial jet with $U_c / U_0 = 1.48$. At further downstream locations the centreline rms axial fluctuations increase and follow a similar profile shape as the mean axial velocity.

The radial plots of the time averaged mean radial velocity (left) and rms radial velocity (right) are shown in Fig. 4. The mean radial velocity is almost zero at near field axial locations ($x/D=0.5, 2.0, 3.0$) and gradually increases in the far field outside the centreline. A symmetric behaviour for the mean radial velocity appears at most axial locations and its magnitude is mainly determined by turbulent diffusion. The rms radial velocity fluctuation profiles have a small peak value in the region above the annular jet at near field positions ($x/D=0.5, 1.0$) and the value of this gradually increases at $x/D=2.0, 3.0$. The distribution of the rms radial velocity does not show a high peak at near field axial positions and its magnitude is significantly lower than the rms axial velocity. This has also been observed by Ribeiro and Whitelaw (1980). The centreline fluctuations increase in the far field and follow the same distribution shape as the rms axial velocity at $x/D=20$. The axial and radial fluctuations values are much closer at further downstream axial locations.

Fig. 5 shows the shear layer distribution of the coaxial jet. The instantaneous contours of the passive scalar field show both the inner shear layer, situated between inner core and outer core, and the outer shear layer. As seen in both rms axial and radial fluctuations, the peak fluctuation values observed in the inner shear layer are associated with rapid mixing inside the inner mixing region. Fig. 5 reveals that the initial shear layer instabilities are relatively smooth in the near field, but then start to roll-up to form vortices in the intermediate and far field regions. The roll-up of the vortices begins at the tip of the inner potential core and expands rapidly out into axial and radial directions. The captured shear layer and the vortex patterns are consistent with the observation of Dahm et al. (1992) for the same velocity aspect ratio ($U_c/U_0=1.48$). However, Dahm et al. (1992) found various alternative vortex patterns with different dynamic structures over a wide range of inlet velocity aspect ratios.

4.2.2 Scalar Field:

The present work has considered separating initial conditions for the passive scalar mixing. The first case (case 1) simulated the scalar mixing by setting the value to 1 only across the core inlet to the domain, while the second case (case 2) simulated the scalar field development with the initial value set to 1 only across the annular inlet. Both simulations have been run independently and separate statistics were collected for time averaged calculations.

Figs. 6 and 7 show sections through the filtered passive scalar and corresponding passive scalar isosurfaces respectively for case 1. Fig. 6 shows the near field passive scalar exhibits little mixing and slow development due to the high core jet velocity

and thus exists less vortex structures in the near field. Fig. 6 and 7 further reveal that the passive scalar mixing gradually increases in the intermediate region and different vortex patterns form that spread radially at downstream axial locations. The subsequent development of the shear layers in the intermediate region appear to be dominated by the vortical eddy structures which form and influence the passive scalar distribution in the intermediate region. The roll up of the passive scalar vortices and the passive scalar distribution remain axi-symmetric. The equivalent sectional filtered passive scalar and isosurface plots for case 2 are shown in Figs. 8 and 9.

Fig. 10 shows the time averaged mean passive scalar at different axial locations. The solid line indicates the radial plots of the mean passive scalar for case 1 and the dashed line indicates the same variable for case 2. The mean passive scalar exhibits the expected Gaussian shape. The radial profile development for case 1 shows less mixing at upstream positions ($x/D=0.5, 1.0, 2.0, 3.0, 5.0$). The radial spread of the passive scalar then starts to increase towards the far field, developing smoothly at downstream positions. The radial scalar profiles in case 2 also shows a gradual increase in the mixing rate towards the far field. However the mixing for the two cases shows some differences at far field axial locations. For example, the case 1 peak value is much higher than case 2 at intermediate regions such as $x/D=5.0, 10.0$, but case 2 profiles have higher values than case 1 further downstream, $x/D=20.0, 30.0$. Much of the mixing for both cases takes place in the developing region including the potential cores as has been observed by Champagne and Wygnanski (1971) in their similar coaxial jet experiment. One can assume that significant intermittency in both velocity and passive scalar fields should occur in these regions and the investigation of probability density distributions and intermittency profiles for both velocity and

passive scalar would thus provide useful further details of the mixing processes. Therefore the next section discusses the intermittency of both the velocity and scalar fields using the numerical data extracted from the simulated turbulent coaxial jet.

4.3 Analysis of results for intermittency fields

Turbulent shear flows with free boundaries displays an intermittent character especially closer to the outer edge of the flow where the flow alternate between rotational and irrotational states. The study of turbulent intermittency is important for many applications such as boundary layer transition in modern turbines and aerofoils, ignition of combustion devices and environmental emissions. The majority of existing turbulence models were originally derived for fully developed flows and thus exhibit some deficiencies in the inhomogeneous intermittent regions near the outer edge of such flows which contaminated with irrotational flow. Therefore detailed understanding of the applicability of existing turbulence models in large eddy simulation for turbulent intermittency is essential and timely. Here we study the calculated probability density functions and radial intermittency plots for the velocity and passive scalar fields using the dynamic sub-grid LES model.

The mathematical derivation for intermittency can be expressed using an indicator function with the value of one in turbulent regions and zero in non-turbulent (laminar) regions. It represents the fraction of time interval during which a point is inside the turbulent fluid. Andreotti (1999) experimentally tested and demonstrated a technique called the normalised histogram method for determine the associated probability density function (PDF). From this, the intermittency value can be calculated using a summation of probability values for a given threshold value. To calculate the

intermittency from PDF's here we used the method proposed by Schefer and Dibble (2001) in which it is assumed that the PDF is smooth at the scale of one histogram bin. Here 8000 measurements at each spatial location with 50 bins over $3-\sigma$ limits of data are considered. Therefore the normalised PDF's can be written as

$$\int_0^1 P(f) df = 1 \quad (8)$$

The intermittency value γ (Gamma) can be calculated from the probability values respect to considered threshold value such that

$$\gamma = P(f > f_{th}) \quad (9)$$

4.3.1 Velocity Field Intermittency:

Here we discuss the probability density function (PDF) and radial intermittency profiles for the velocity at different downstream axial locations. Fig. 11 shows the probability density distributions of instantaneous axial velocity at $x/D=20$ (a-c) and $x/D=30$ (d-f). The pdf of axial velocity follows Gaussian shape on the centreline and close to the centreline, but changes from a Gaussian distribution to delta function at far radial locations. The intermediate region from Gaussian to delta shape can be identified as a highly intermittent region where frequent switches from rotational to irrotational behaviour happen. As the present discussion is focused on a coaxial jet, the variation of pdfs from Gaussian to delta starting from the centreline to far radial locations at given axial distance can change with velocity aspect ratio U_c/U_0 . Fig.11 (d)-(f) show the pdfs of velocity at $x/D=30$ and a similar observation can be made for the pdf shapes with respect to radial distance. Again the pdf shapes change from Gaussian to delta with increased radial distance, but discrepancies are apparent for pdf shapes between the two axial locations, $x/D=20$ and $x/D=30$. For example, Fig 11. (b)

and (e) show the pdfs of axial velocity at the same radial location for $x/D=20$ and 30. The pdf shape of Fig. 11 (b) exhibit a less Gaussian shape, but not a delta function shape and thus define a region indicates of more intermittent behaviour. By comparison the pdf shape of Fig. 11 (e) is already closer to delta shape and thus indicates less intermittent behaviour compare with Fig. 11 (b). To analyse this particular finding we have also considered radial intermittency profiles. In this case the velocity intermittency is calculated from the probability density distribution of the instantaneous velocity. For velocity intermittency calculation, we used a threshold value of 13.1 m/s which is equal $(U_c + U_a)/10$.

The radial variation of the velocity intermittency at $x/D=10, 20$ and 30 is shown in Fig.12. The intermittency value is unity close to centreline at all three locations and then starts to reduce with increased radial distance. At $x/D=10$ (Fig 12. a) the intermittency shows a sudden drop and thus as can expect a smaller change between rotational and irrotational vortices. The intermittency gradually increases towards the far field $x/D=20, 30$ close to the outer edge of the flow where the viscous super layer plays a dominant role and thus produces more intermediate values of intermittency between 0 and 1. Finally, the velocity field converts to laminar with respect to threshold value (13.1 m/s) at far radial locations and thus intermittency values fall to zero here.

4.3.2 Scalar Field Intermittency:

In this section we discuss the pdfs and intermittency of the passive scalar field for two considered cases, identified as case 1 and case 2 in the scalar mixing section. Fig.13 (a)-(c) show the passive scalar pdfs at $x/D=20$ and Fig. 13 (d)-(f) show the pdf values

$x/D=30$. Similar pdf variation can be seen at both $x/D=20$ and 30 axial locations. The pdfs of the passive scalar shows more mixing near the centreline region and then follows the delta function with increased radial distance.

The corresponding pdfs of the passive scalar for case 2 are shown in Fig. 14. In this case, the pdf variation shows some differences for the axial locations $x/D=20$ (Fig. 14 a-c) and $x/D=30$ (d-f). The centreline pdf values at $x/D=20$ follow a Gaussian type distribution, while pdfs at $x/D=30$ take an intermediate shape between Gaussian and delta forms. Similar behaviour can be seen in Fig. 14 (b) and (e). However the pdfs follow delta function distribution at the far radial locations for both $x/D=20$ and 30. Fig.15 shows the radial variation of the passive scalar intermittency at $x/D=10, 20$ and 30 for case 1 and case 2. Here intermittency is defined as the fraction of time that passive scalar is greater than a surrounding medium threshold. In this work, we used a passive scalar threshold value 0.015 as proposed by Schefer and Dibble (2001) for their intermittent propane jet.

Comparison between case 1 (circles) and case 2 (gradients) shows these similar at $x/D=10$ and then differences widen at $x/D=20$ and 30. The region near the centreline shows a unit value for the intermittency and thus suggests turbulent mixing is not enough to transport unmixed air into the core region of such a coaxial jet. The intermittency profiles shape is similar for both cases at $x/D=20$, but slight deviation occurs for the intermittency values. Again, similar variation occurs at $x/D=30$. It can also be seen from Fig.12 and 15 that the radial intermittency of passive scalar profiles are consistent with corresponding velocity profiles at their axial locations.

5. CONCLUSION

Simulations for a turbulent coaxial jet with high core and annular jet velocities (with aspect ratio of $U_c/U_0=1.48$) have been conducted using LES. The simulations studied both velocity and passive scalar fields, and the investigation considered both instantaneous and time averaged quantities to describe the flow and mixing fields. The radial plots of mean and rms of velocity field have been discussed and the passive scalar distributions have been separated into two parts in studying the mixing from corresponding simulations with passive scalar introduced initially from the core and annular inlet jets. The mean flow field captured the potential cores and initial self-similar states. The high velocity fluctuations occurring inside the inner mixing regions due to the vortex shedding have also been captured by the present simulation. The time averaged mean scalar distributions exhibited similarities in the near field and differences in the far fields for the two cases. The calculated velocity fluctuations resulted in intermittent behaviour near the jet boundaries for both velocity and passive scalar fields. The probability density functions and radial intermittency plots obtained describe the balance between the rotational irrotational states for a given threshold value and thus shows a significance of intermittency close to outer edge of the flow.

Acknowledgment

This work was supported by the EPSRC funding under grant EP/E036945/1 on the Modelling and Simulation of Intermittent Flows. We also acknowledge the support provided by the HEIF 3 OMEGA project for the initial phase of this work.

REFERENCES

Akselvoll, K, Moin, P, 1996, Large eddy simulation of turbulent confined coannular jets, *J. Fluid Mechanics*, 315, 387-411.

Balarac, G, Metais, O, 2005, The near field of coaxial jets, 2005, *Phys. Fluids*, 17, 065102-1-14.

Balarac, G, Si-Ameur, M, Lesieur, M, Metais, O, 2007, Direct numerical simulations of high velocity ratio coaxial jets: mixing properties and influence of upstream conditions, *J. Turbulence*, 8 (22), 1-14.

Becker, H.A, Hottel, H.C, Williams, G.C, 1965, Concentration intermittency in jets, *Tenth Symp. Combust.*, The Combustion Institute.

Bilger, R.W, Antonia, R.A, Sreenivasan, K.R, 1976, Determination of intermitency from the probability density function of a passive scalar, *Phys. Fluids*, 19 (10), 1471-1474.

Boersma, B.J, Lele, S.K, 1999, Large eddy simulation of a Mach 0.9 turbulent jet, *AIAA* 99-1874.

Buresti, G, Petagna, P, Talamelli, A, 1998, Experimental investigation on the turbulent near-field of coaxial jets, *Exper. Therm. Fluid Sci.*, 17, 18-26.

Byggstoyl, S, Kollmann, W, 1981, Closure model for intermittent turbulent flows, Int. J. Heat and Mass Transfer, 24(11), 1811-1822.

Chigier, N. A. and Beer, J. M., 1964, The Flow Region Near the Nozzle in Double Concentric Jets, Trans. ASME, J. Basic Eng., 86, 797-804.

Cho, J.R, Chung, M.K, 1982, A $k - \varepsilon - \gamma$ equation turbulence model, J. Fluid Mech., 237, 301-322.

Champagne, F. H. and Wygnanski, I. J., 1971, An Experimental Investigation of Coaxial Turbulent Jets, Int. J. Heat Mass Transfer, 14, 1445- 1464.

Dahm, W. J. A., Frierler, C. E. and Tryggvason, G., 1992, Vortex Structure and Dynamics in the Near Field of a Coaxial Jet, J. Fluid Mech., 241, 371-402.

da Silva C B and M'etais O, 2001, Coherent structures in excited spatially evolving round jets Direct and Large-Eddy Simulation Volume 4, Kluwer Academic Pub., New York.

da silva, C.B, Balarac, G, Metais, O, 2003, Transition in high velocity ratio coaxial jets analysed from direct numerical simulations, J. Turbulence, 4, 1-18.

Dianat, M, Yang, Z, Jiang, D, Mcguirk, J.J, 2006, Large eddy simulation of scalar mixing in a coaxial confined jet, Flow Turb. Combustion, 77, 205-227.

Forstall, W, and A.H.Shapiro, 1951, Momentum and mass transfer in coaxial gas jets, J. Applied Mechancis, 18, 219-223.

Garnier, F., Baudoin, C., Woods, P. and Louisnard, N, 1997, Engine emissions alteration in the near field of an aircraft, J. Atmos. Environ. 31, pp.1767-1781.

Ko, N.W.M, Kwan, A.S.H, 1976, The initial region of subsonic coaxial turbulent jets, J. Fluid Mech., 73, 305-332.

Kollomann, W, Janicka, J, 1982, The probability function of a passive scalar in turbulent shear flows, Phy. Fluids, 25(10), 1755-1769.

Kwan, A.S.H, Ko, N.W.M, 1977, The initial region of subsonic coaxial jets, Part 2, J. Fluid Mech., 82, 273-287.

Kenzakowski D.C, Papp J.L, Dash S.M, 2002, Modeling turbulence anisotropy for jet noise prediction. AIAA Paper 2002-0076.

Kenzakowski D.C, Papp J.L, 2005, EASM/J extensions and evaluation for jet noise prediction. AIAA Paper 2005- 0419.

Kirkpatrick, M.P., Armfield, S.W. and Kent J.H., 2003a, A representation of curved boundaries for the solution of the Navier-Stokes equations on a staggered three-dimensional Cartesian grid, J. of Comput. Physics 184, 1-36.

Kirkpatrick, M.P., Armfield, S.W., Masri, A.R. and Ibrahim, S.S., 2003b, Large eddy simulation of a propagating turbulent premixed flame, *Flow Turb. Combust.*, 70 (1) 1-19.

Kirkpatrick, M.P. and Armfield, S.W., 2005, Experimental and large eddy simulation results for the purging of a salt water filled cavity by an overflow of fresh water, *Int. J. of Heat and Mass Transfer*, 48 (2), 341-359.

Leonard, B.P., 1987, SHARP simulation of discontinuities in highly convective steady flows, *NASA Tech. Memo.*, Vol. 100240.

Piomelli, U. and Liu, J., 1995, Large eddy simulation of channel flows using a localized dynamic model, *Phy. Fluids* 7, 839-848.

Ribeiro, M.M, Whitelaw, J.H, 1980, Coaxial jets with and without swirl, *Journal of Fluid Mechanics*, 96, 769-795.

Ranga Dinesh K.K.J., 2007, Large eddy simulation of turbulent swirling flames. PhD Thesis, Loughborough University, UK.

Sadr, R, Klewicki, J, 2003, An experimental investigation of the near field flow development in coaxial jets, *Phy. Fluids*, 15 (5), 1233- 1246.

Schefer, R.W, Dibble, R.W, 2001, Mixture fraction field in a turbulent nonreacting propane jet, *AIAA J.* 39, 64-72.

Smagorinsky, J., 1963, General circulation experiments with the primitive equations”,
M. Weather Review 91, 99-164.

Tucker, P, 2008, The LES models role in jet noise, Prog. Aero. Sci. 44, 427-436.

Wynanski, I, H.E.Fiedler, H.E, 1969, Some measurements in the self preserving jet,
J. Fluid Mech. 38, 577-612.

Yuan, L.L, Street, R.L, Ferziger, J.H, 1999, Large eddy simulation of a round jet in
cross flow, J. Fluid Mech. 379, 71-104.

FIGURE CAPTIONS

Fig. 1. LES calculated mean axial velocity, rms axial velocity and mean mixture fraction at different axial locations using different grid resolutions. Dashed lines represent the Grid 1 results (1.2 million grid points), and solid lines represent the Grid 2 results (2.4 million grid points)

Fig. 2. Contour plot of time averaged mean axial velocity

Fig. 3. Radial plots of time averaged mean axial velocity (left side)) and rms axial velocity (right side) at different axial locations

Fig. 4. Radial plots of time averaged mean radial velocity (left side) and rms radial velocity (right side) at different axial locations

Fig. 5. LES predicted shear layer for the coaxial jet, contours of instantaneous passive scalar (contour levels are 0.05 to 0.9)

Fig. 6. Snapshot of passive scalar at cross plane for case 1

Fig. 8. Snapshot of passive scalar at cross plane for case 2

Fig. 9. Isosurfaces of passive scalar for case 2

Fig. 10. Radial plots of time averaged mean passive scalar at different axial locations, solid line indicates case 1 results and dashed line represents case 2 results

Fig. 11. PDF of velocity at (a), (b), (c) $x/D=20$, and (d), (e), (f) $x/D=30$

Fig. 12. Radial variation of the velocity intermittency at, a) $x/D=10$, b) $x/D=20$, c) $x/D=30$

Fig. 13. PDF of passive scalar at (a), (b), (c) $x/D=20$, and (d), (e), (f) $x/D=30$ for case 1

Fig. 14. PDF of passive scalar at (a), (b), (c) $x/D=20$, and (d), (e), (f) $x/D=30$ for case 2

Fig. 15. Radial variation of the passive scalar intermittency at, a) $x/D=10$, b) $x/D=20$, c) $x/D=30$ for case 1 and case 2. Here circles indicate results for case 1 and gradient symbol indicate results for case 2

FIGURES

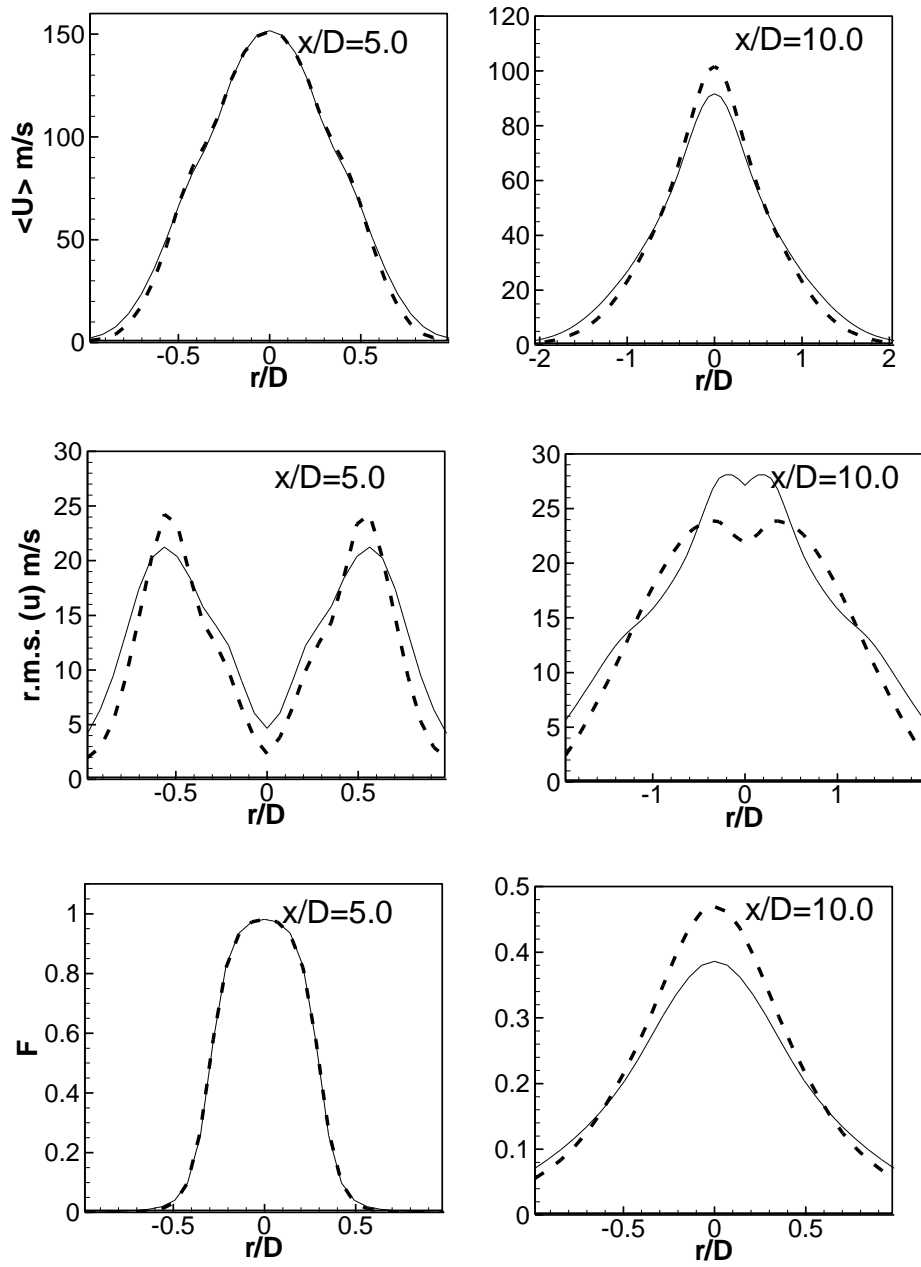


Fig. 1. LES calculated mean axial velocity, rms axial velocity and mean mixture fraction at different axial locations using different grid resolutions. Dashed lines represent the Grid 1 results (1.2 million grid points), and solid lines represent the Grid 2 results (2.4 million grid points)

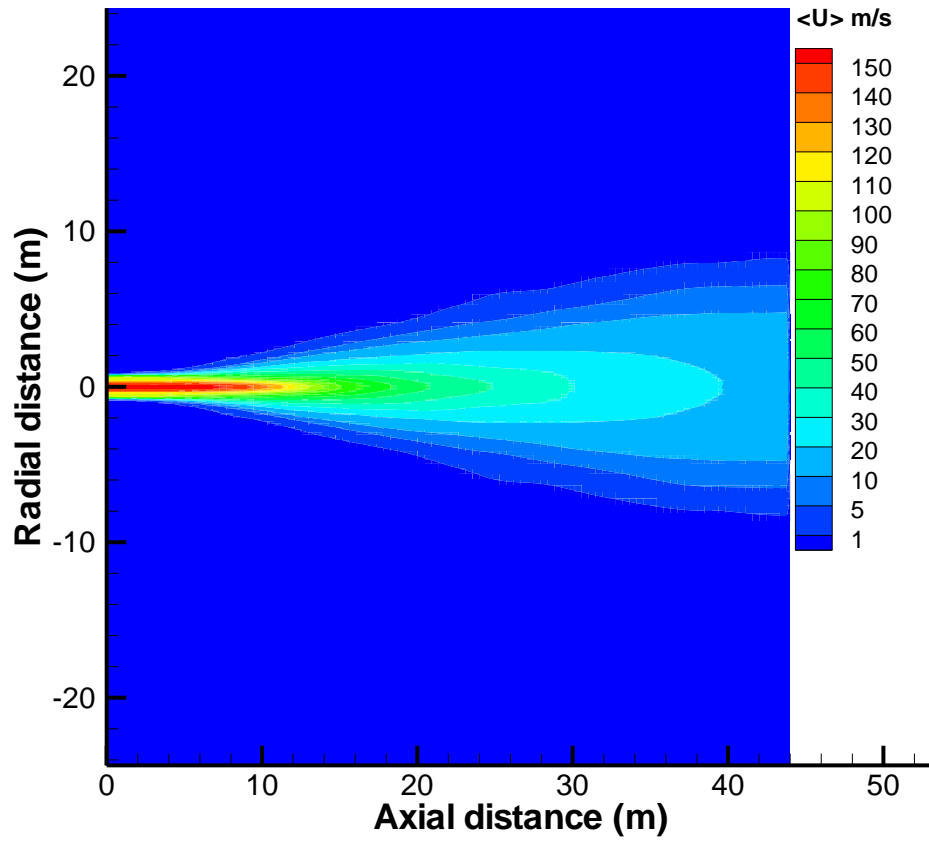


Fig. 2. Contour plot of time averaged mean axial velocity

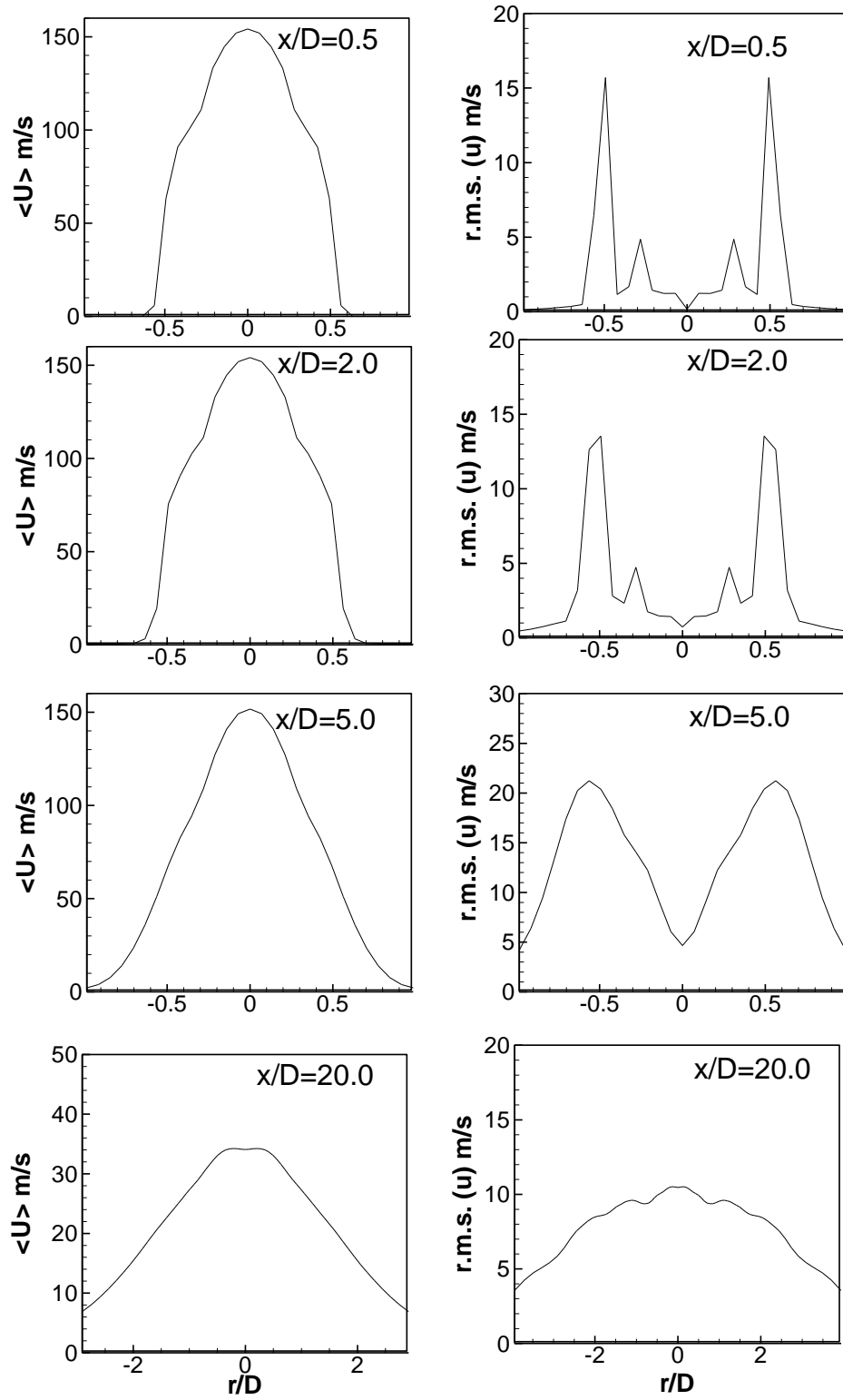


Fig. 3. Radial plots of time averaged mean axial velocity (left side)) and rms axial velocity (right side) at different axial locations

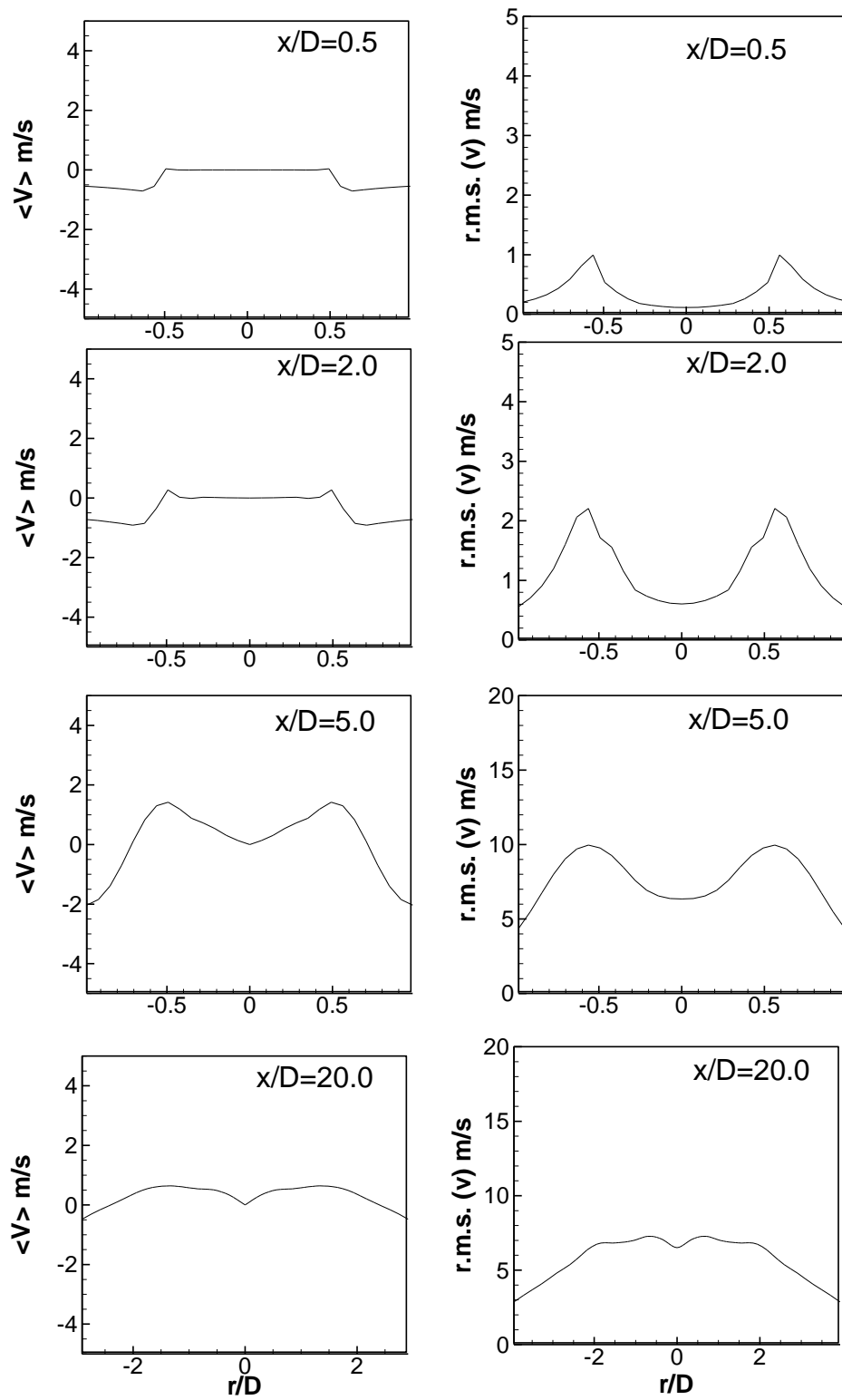


Fig. 4. Radial plots of time averaged mean radial velocity (left side) and rms radial velocity (right side) at different axial locations

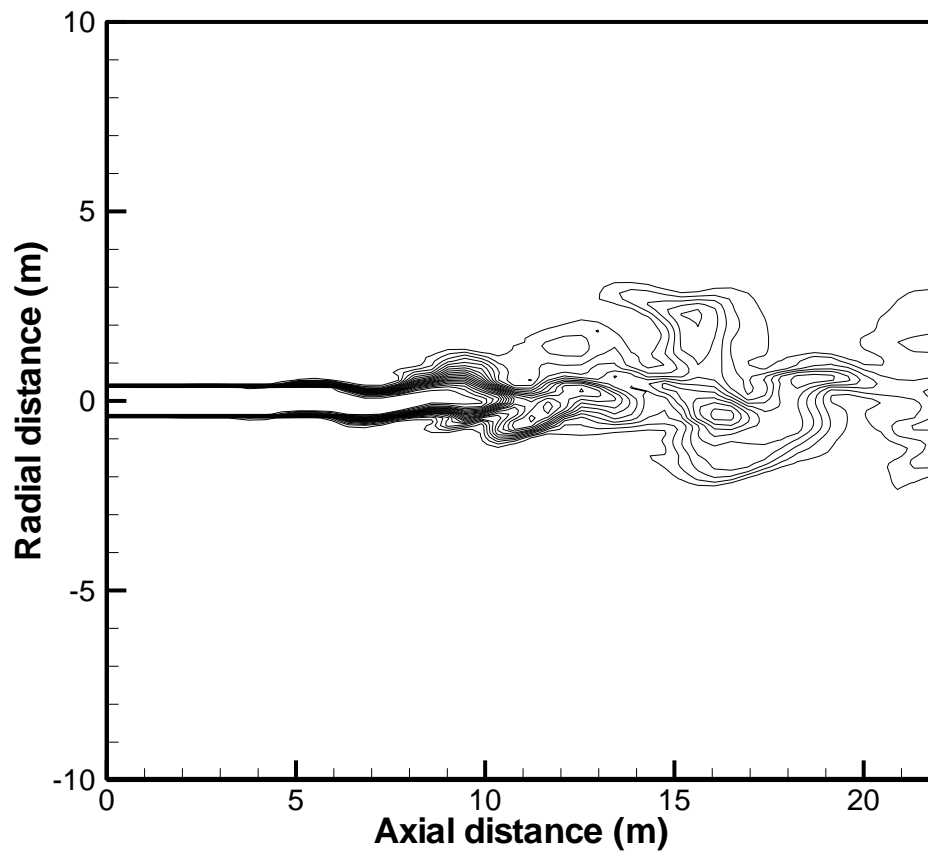


Fig. 5. LES predicted shear layer for the coaxial jet, contours of instantaneous passive scalar and contour levels are 0.05 to 0.9

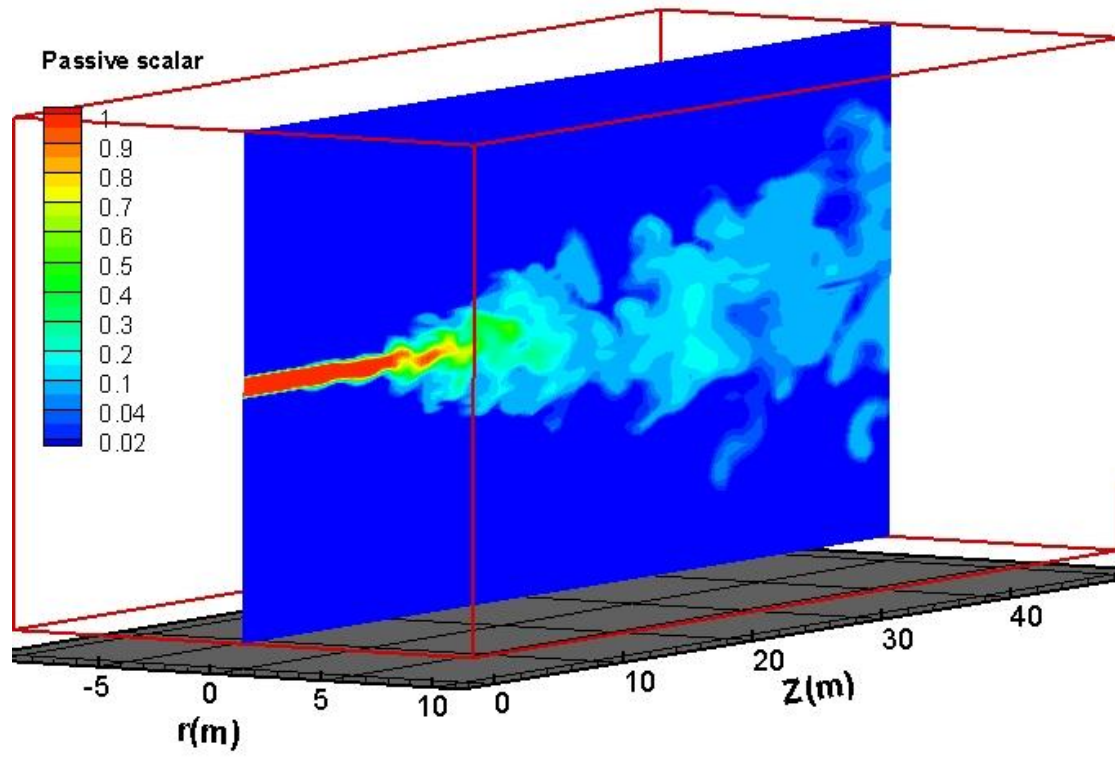


Fig. 6. Snapshot of passive scalar at cross plane for case 1

Passive scalar
Iso values are 0.05,0.5,1.0

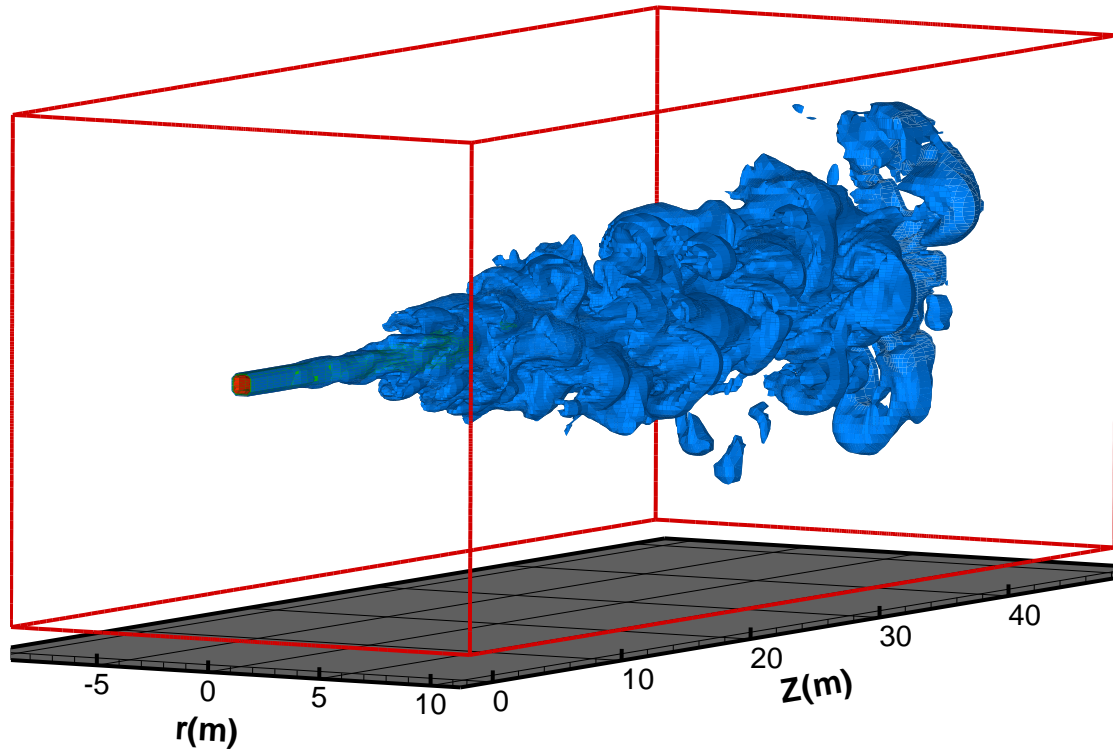


Fig. 7. Isosurfaces of passive scalar for case 1

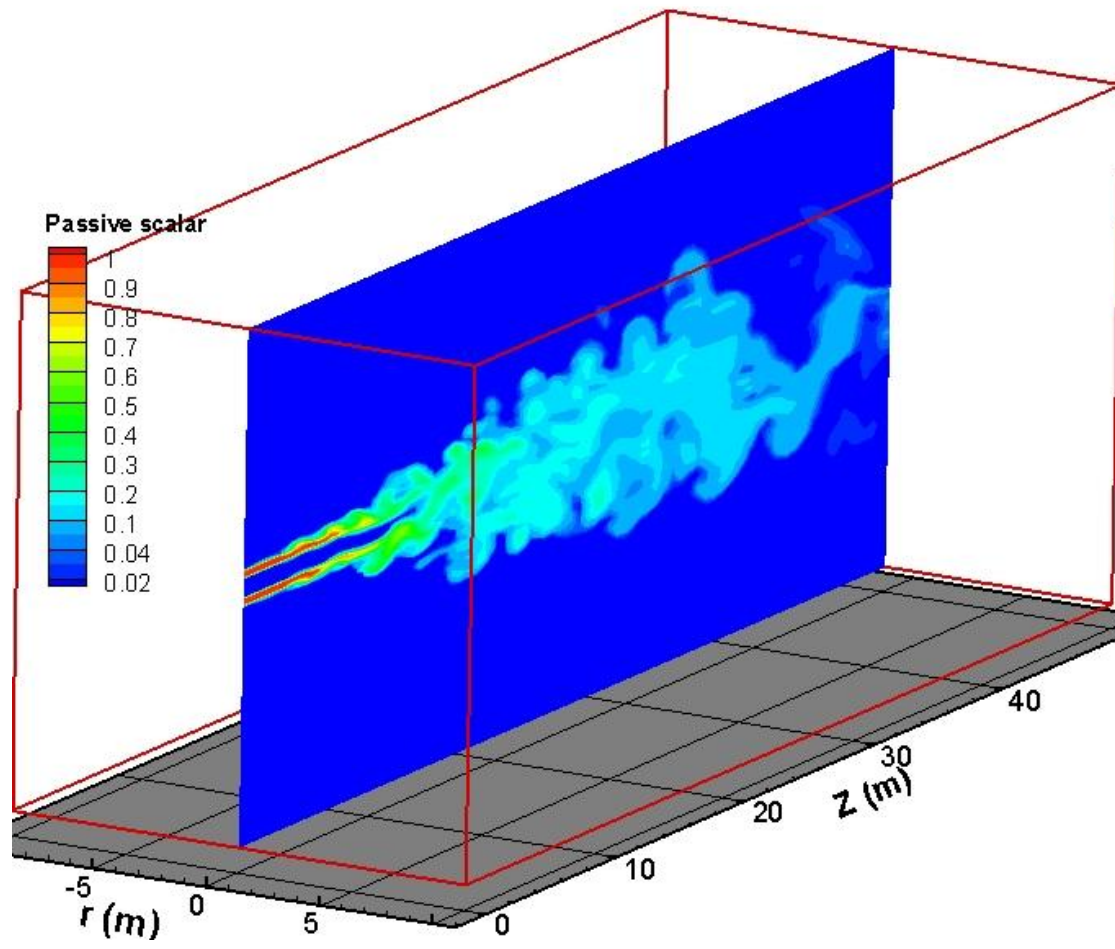


Fig. 8. Snapshot of passive scalar at cross plane for case 2

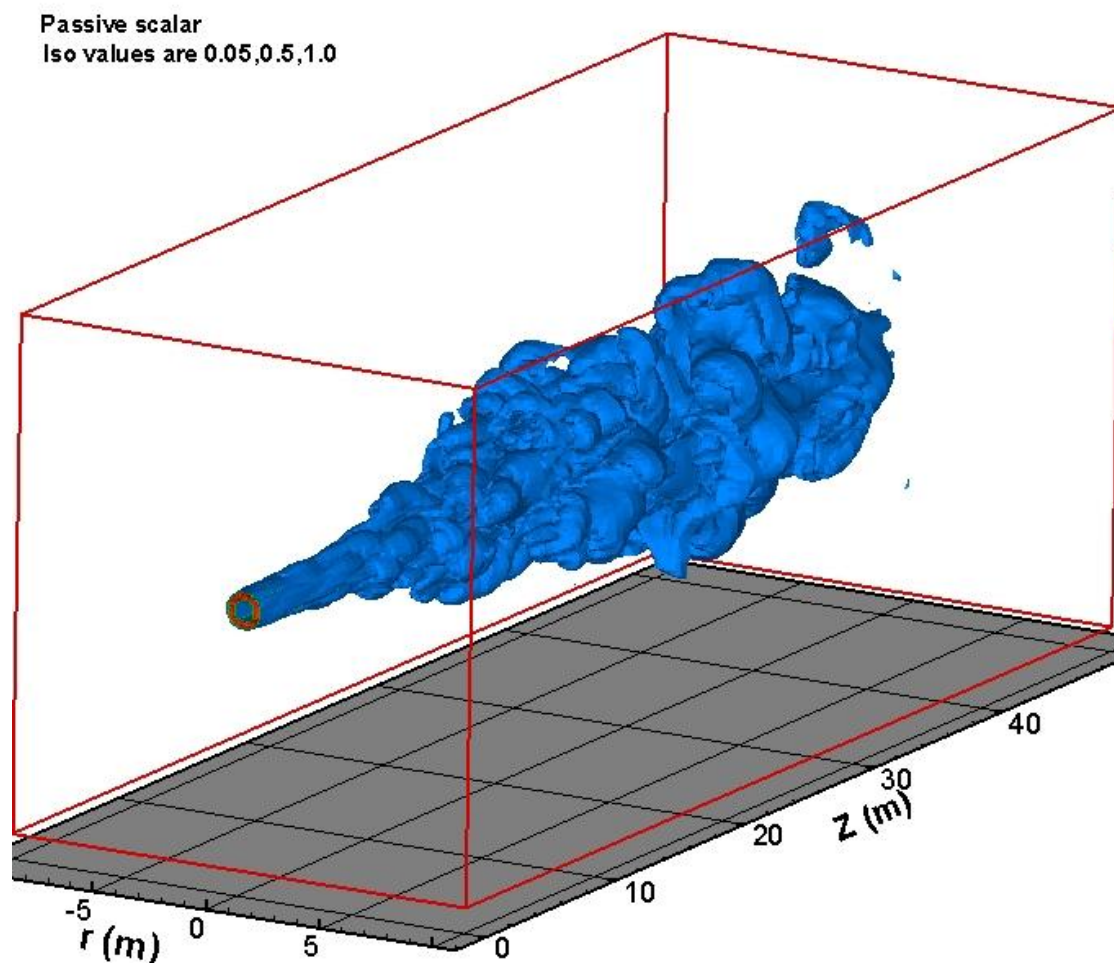


Fig. 9. Isosurfaces of passive scalar for case 2

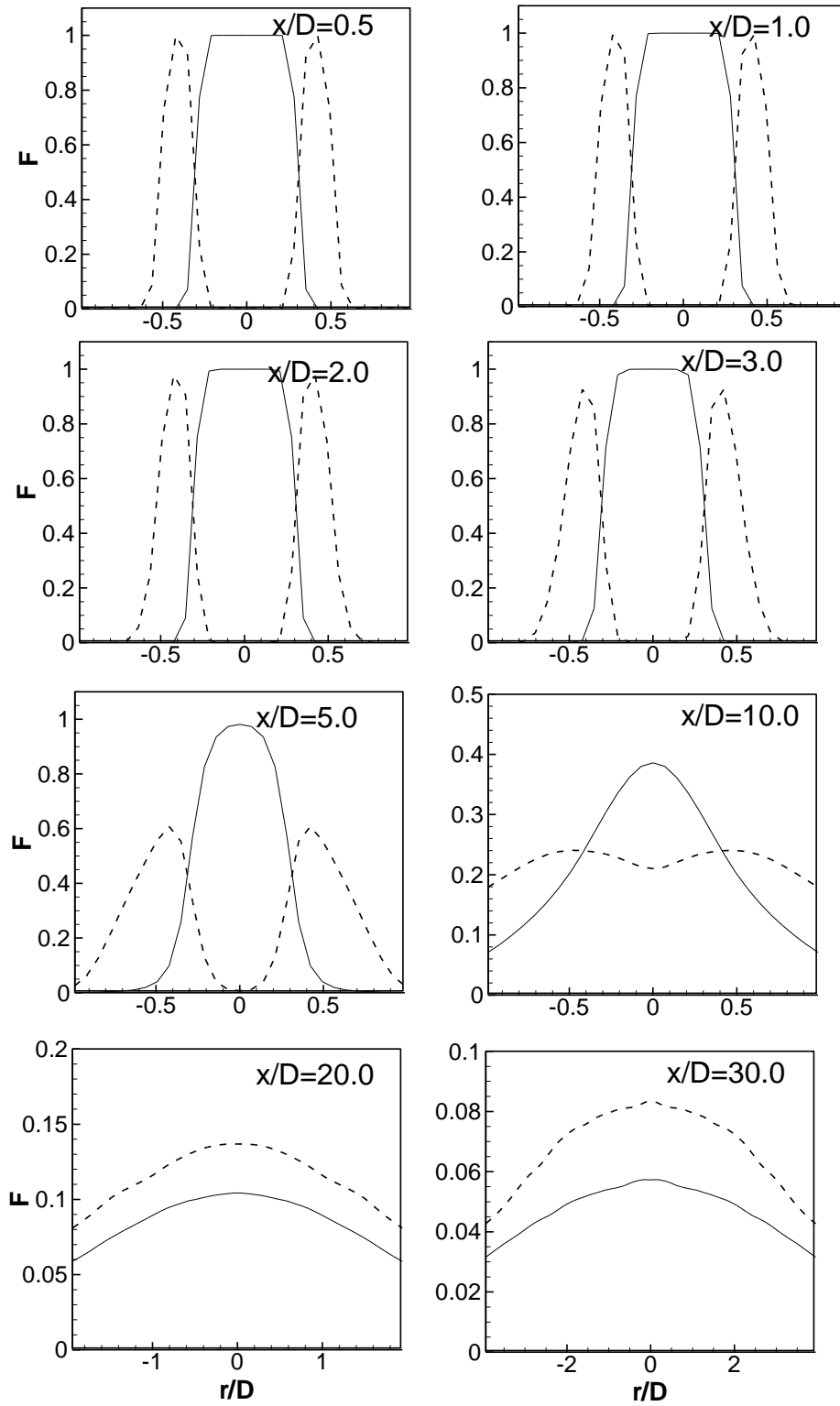


Fig. 10. Radial plots of time averaged mean passive scalar at different axial locations, solid line indicates case 1 results and dashed line represents case 2 results

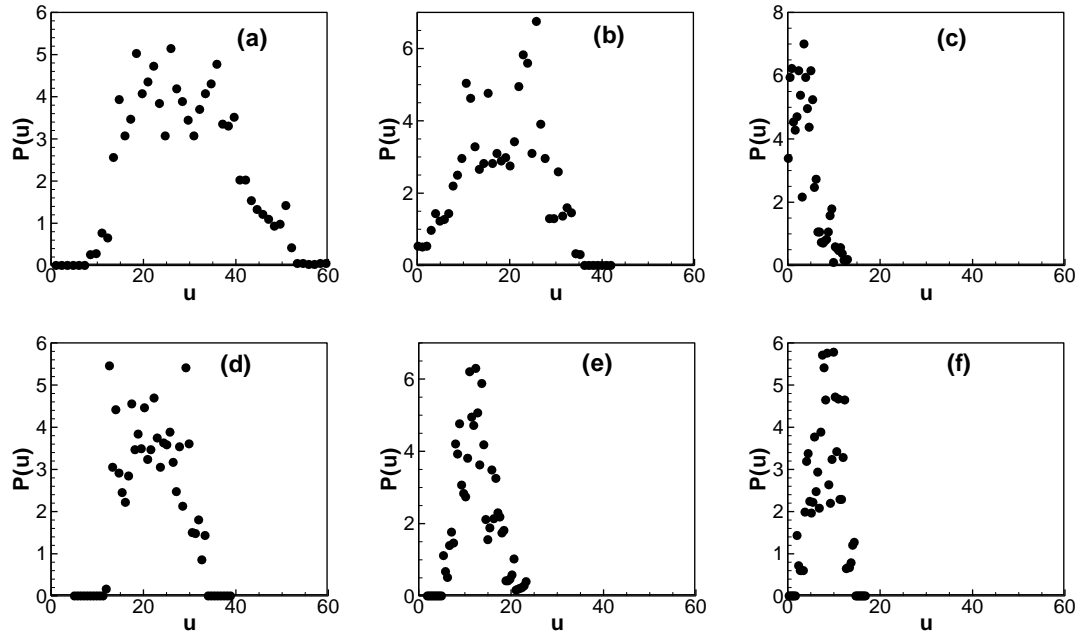


Fig. 11. PDF of velocity at (a), (b), (c) $x/D=20$, and (d), (e), (f) $x/D=30$

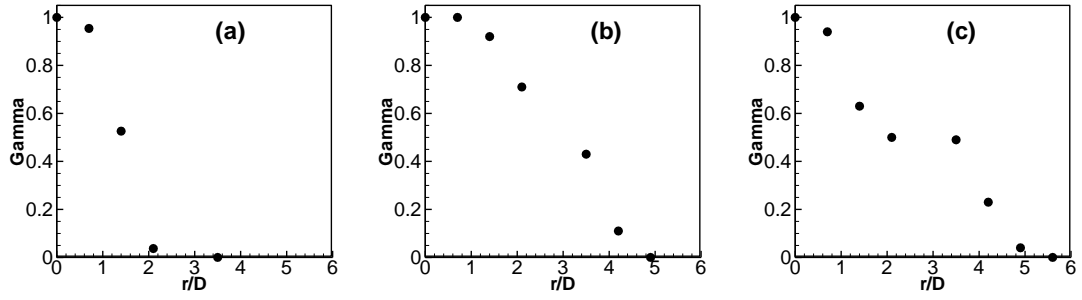


Fig. 12. Radial variation of the velocity intermittency at, a) $x/D=10$, b) $x/D=20$, c) $x/D=30$

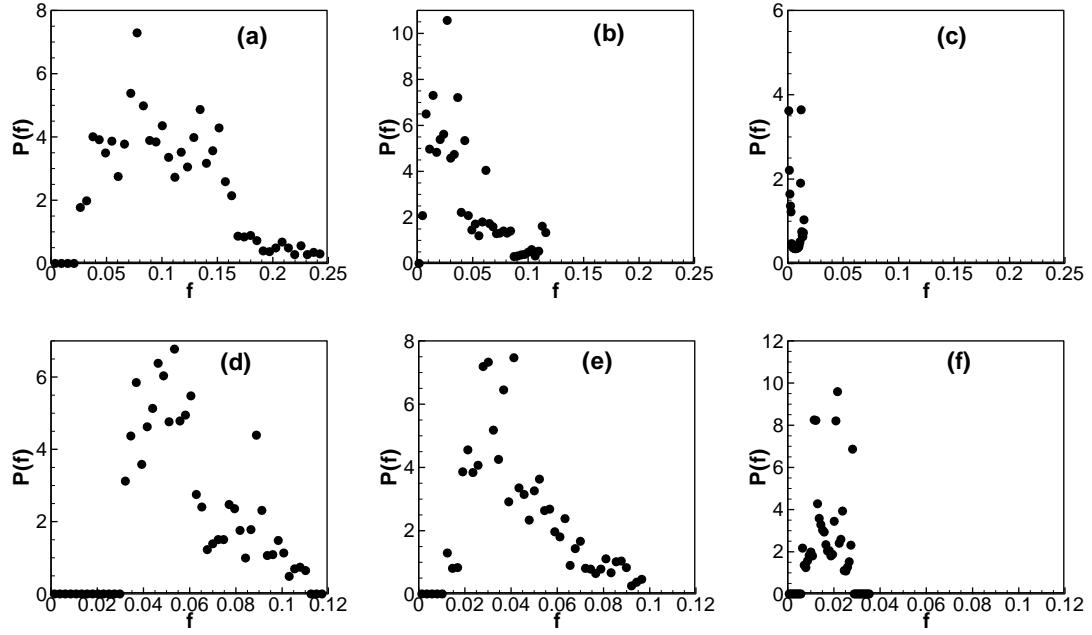


Fig. 13. PDF of passive scalar at (a), (b), (c) $x/D=20$, and (d), (e), (f) $x/D=30$ for case 1

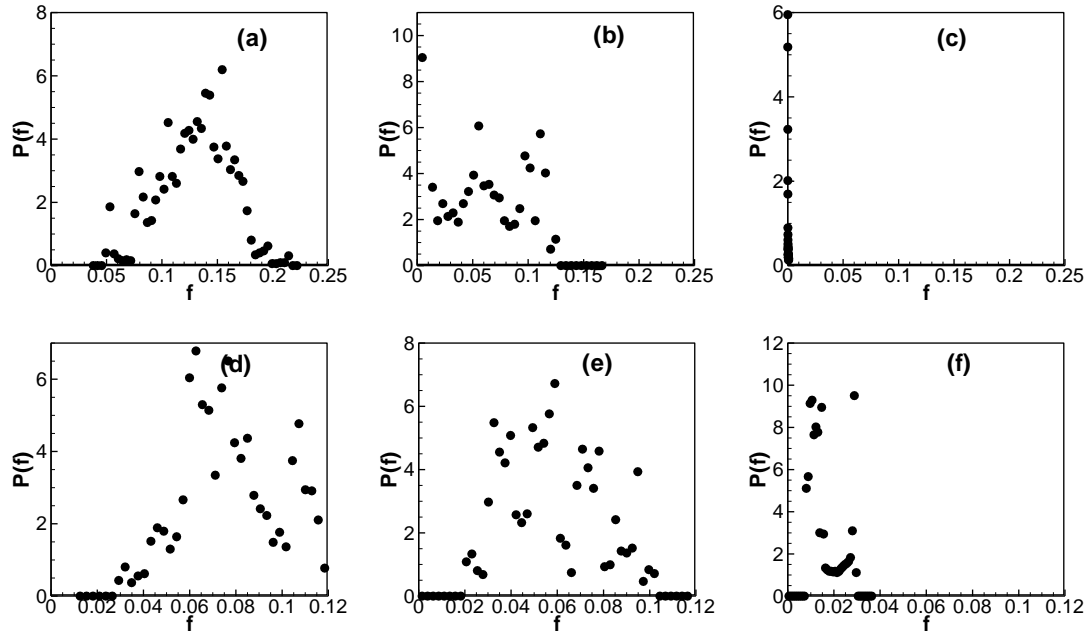


Fig. 14. PDF of passive scalar at (a), (b), (c) $x/D=20$, and (d), (e), (f) $x/D=30$ for case 2

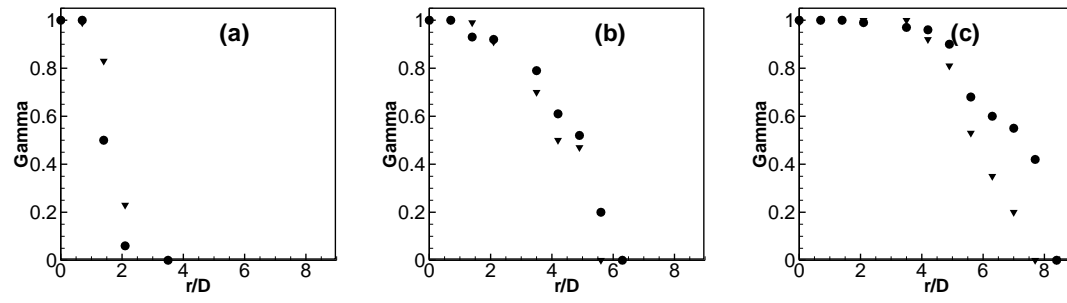


Fig. 15. Radial variation of the passive scalar intermittency at, a) $x/D=10$, b) $x/D=20$, c) $x/D=30$ for case 1 and case 2. Here circles indicate results for case 1 and gradients indicate results for case 2